Toward a multi-physical approach to connection ageing in power modules

Guillaume Pellecuer, François Forest, Jean-Jacques Huselstein, Thierry Martiré, Olivier Arnould, André Chrysochoos

Toward a Multi-Physical Approach to Connection Ageing in Power Modules

G. Pellecuer [(1)], F. Forest [(1)], J.-J. Huselstein [(1)], T.Martiré [(1)]
O. Arnould [(2)], A. Chrysochoos [(2)]

[(1)] Institut d'Electronique et des Systèmes, Université de Montpellier, CNRS Montpellier, France,
[(2)] Laboratoire de Mécanique et Génie Civil, Université de Montpellier, CNRS Montpellier, France
Corresponding author: Guillaume Pellecuer – guillaume.pellecuer@umontpellier.fr

ABSTRACT – Generally, studies on ageing of power module have very often sought to write phenomenological laws able to give an estimate of their lifespan. These laws, identified experimentally, are empirical functions of the characteristic electrical loads that the component must withstand. As an alternative, this paper presents a first attempt of numerical approach for wire bond ageing in semiconductor power modules that takes account for the different multi-physical coupling mechanisms that occur during the component life. The electro-thermal and thermo-mechanical interactions are physically described and numerically modeled. The calculations show important viscoplastic strains in the connection zones and bonding wires from the first loading cycles. A quasi-cyclic stabilization of the mechanical and thermal states is observed at more than a hundred cycles (viscoplastic shakedown). The creep-fatigue damage mechanisms become then preponderant inducing mechanical-electrical couplings.

Keywords—— Reliability, IGBT Power Modules, Power Cycling, Thermomechanical Fatigue, Wire bonds.

1. INTRODUCTION TO THE POWER MODULE AGEING

Semiconductor power modules are key devices in power electronics. They are used in many applications where reliability is an essential concern, such as network interconnections, transportation, and critical infrastructure. In many cases, these devices are subjected to repetitive variations of electrical loading conditions that induce thermal cycling on integrated dies due to their resulting self-heating (Joule effects). Indeed, the modules mainly consists of different stacked material layers through which the heat diffuses, thereby generating significant, non-stationary temperature gradients. The presence of this induced thermal loading within a multilayer structure with varying expansion coefficients thus generates mechanical stresses and consequently the conditions for ageing mechanisms to appear. Experiment shows that the latter mainly affect the upper zone of the components, i.e., the bonds between the wires and the metallization of the emitter. (Fig. 1) [1][2][3].

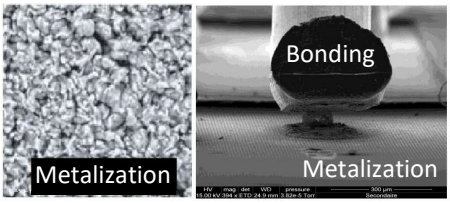

Fig. 1 : SEM images of metalization degration (left) and wirebond lift off (right)

1.1. *Studied power module*

The component studied in this paper is an IGBT (Insulate Gate Bipolar Transistor) power module representative of the today technology [4][5]. It is the MICROSEMI APTGT200A60T3AG 600V-200A module (Fig. 2). This module is made of 2 IGBT chips and 4 diodes forming an inverter arm. An elementary switch consists of one IGBT and 2 diodes associated in parallel.

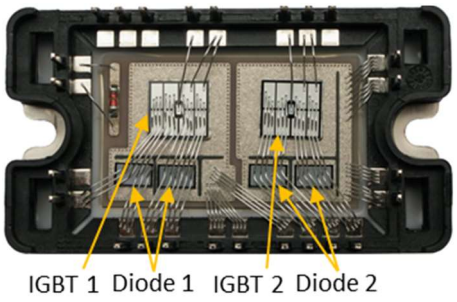

Fig. 2 : IGBT Power Module used as test sample

The ageing study of this kind of power modules can be developed following two paths. First, via an experimental approach, lifespan's curves are established on the basis of industrial feedback or on experimental data provided by specially designed test benches. Secondly, it consists of analyzing physically and modeling numerically the different electro-thermo-mechanical mechanisms leading to the degradation of modules.

1.2. *Experimental approach*

Many ageing studies of power semiconductor modules are carried out using test benches [6][7]. IES (Institut d'Électronique et des Systèmes) institute has developed test benches to place IGBT power modules under realistic power cycling conditions, notably with highly adjustable test parameters. Results have been obtained on different types of modules and with various electrical stresses and thermal conditions. They have highlighted interesting trends such as time/frequency dependence [2][8]. The test benches (Fig. 3) implemented to provide the experimental results presented below have been described in previous papers [2][9][10]. The components under test are IGBT inverter arms that are combined in a full bridge. They share an inductive load allowing them to be tested under a wide range of conditions using the opposition method [9]. Due to the

back-to-back operating mode of the two legs, power consumption is limited to the inverter losses. The corresponding PWM control part enables setting various shapes of IGBT currents and, consequently, various power cycling shapes.

Fig. 3 : Test benches

Throughout the tests, the on-state voltage V_{CE} across each chip is measured periodically for given current and junction temperature conditions [11]. This allows detecting damage occurring on the wire bond junctions that can be revealed by a low, but measurable, increase in this voltage. Tests are stopped when the voltage increase reaches 3% to 5% of the initial on-state voltage. An increase in V_{CE} of 3% compared to its initial value before ageing corresponds to a critical state where a quarter of the bonding wires can be peeled off [11][12]. Indeed, above 3%-5%, the growth of the voltage V_{CE} is very fast and during the next few thousand cycles the component is completely destroyed and analysis becomes impossible. In some rare instances, failure occurs before the detection of such an increase, in which case the sample cannot be considered when analyzing results.

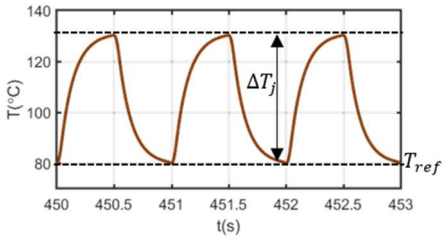

Fig. 4 : Example of stabilized thermal cycles of IGBT die

Lifetime is defined as the number of thermal cycles (Fig. 4) reached until this on-state voltage increases by 3-5%. The damaged modules are then opened, the silicone gel is removed and the top part of the dies is observed using an SEM. In all tested samples, the lift-off of wire bonds (3 to 8 per die in Fig. 5) is the only kind of damage that occurs.

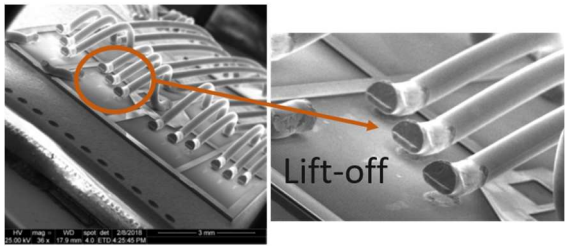

Fig. 5 : View of lift-off in a tested sample

The results are then used to establish lifespan curves as a function of thermal loading conditions. This statistical approach in the form of an empirical model then allows the definition of laws that can be used by manufacturers or customers.

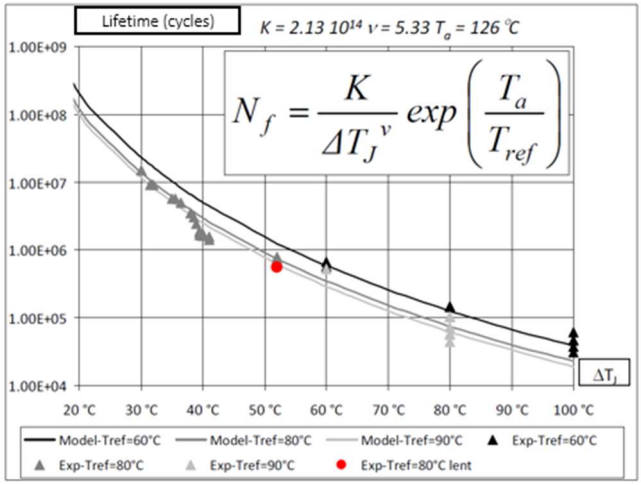

Fig. 6 : Life time curves : experimental and Held Law comparison

In Fig. 6, an example of results obtained in previous work are compiled to establish a Held model [13]. This latter allows one to estimate the lifetime as a function of the amplitude of the thermal cycling ΔT_J and the low temperature of the T_{ref} cycle. There are other laws more commonly used to describe the lifetime of power modules such as Coffin-Masson's law [14][15]. This law, which is widely used to describe module fatigue, is often modified to include the influence of parameters such as temperature rise time or cycling frequency [16][17]. These laws are generally identified for given modules. They do not, a priori, allow one to predict a lifespan in the case of others IGBT module brands (not yet tested in fatigue), or of known modules overcoming more severe electric conditions than those already imposed.

1.3. Motivation

As previously underlined, the experimental study of the ageing of power semiconductor modules is an essential asset to highlight and understand the mechanisms responsible for failures. It also allows to establish laws based on empirical models which have the advantage of directly linking the lifetime of the modules to the thermal loads experienced by the component, as mentioned above.

However, this pragmatic method does not attempt to consider all the physical mechanisms responsible for the ageing of the modules. To take a step forward in understanding mechanisms leading to the modules ageing, the different physics occurring during its lifespan must be considered, trying to take their interactions and their irreversible character into account. Several articles on this topic have already been proposed in the literature [18][19][20], and it is in this perspective that this work is carried out. Through numerical modelling, all the multi-physical interactions are successively considered, with the ultimate aim of better quantify the intensity of these interactions and get better prediction of the module's lifespan for a large domain of electrical loadings.

2. THERMOMECHANICAL MODELING BACKGROUND

The starting point of this modelling is the determination of the electrical dissipation sources. Indeed during their operating, the power modules are the seat of time-dependent Joule effects (conduction and switching losses) [8]. The induced distribution of heat sources generates a self-heating which creates, via thermal expansion mechanisms, mechanical stresses (see Fig. 7). If the stress intensity reaches the yield stress, viscoplastic strains occur during each thermal cycle (low cycle fatigue) inducing creep and/or positive/negative hardening leading rapidly the solder wire bond to the failure. When stress paths remain within the so-called elastic domain, electric loadings induce a more gradual degradation of the matter named high cycle fatigue mechanisms. Whatever the fatigue mechanisms involved, it is highly likely that the progressive and heterogeneous evolution of the microstructure damage modifies the distribution of electric current densities within the component and reinforces the heterogeneous character of the heat sources and thus of the temperature gradients and stress intensities, thus accelerating the degradation process. In Fig. 7 an illustration of these different couplings is basically shown.

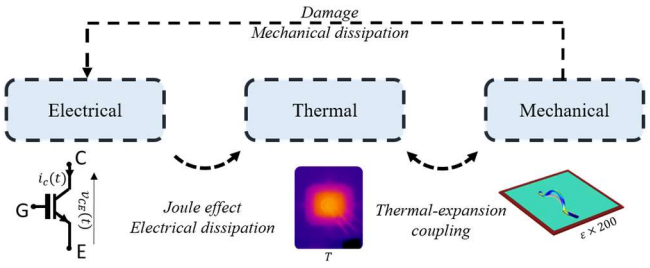

Fig. 7 : Basic sketch of multiphysical couplings inducing fatigue, leading lift-off of the wire bond

The objective of this work was therefore to identify, model, and simulate the electro-thermo-mechanical interactions appearing on the wire bond/die interface. In a first stage, we considered the electro-thermal couplings and the thermomechanical mechanisms until a viscoplastic stabilization occurred. The next stage will be the consideration of fatigue damage and the influence of the mechanical degradation and the distribution of electric densities.

2.1. Electro-thermo-mechanical context

A power module, used in a converter operating under a variable electrical regime, is the seat of time-varying electrical dissipation (Joule effect). This is the so-called "power cycling".

Due to the thermo-dilatability of the materials used, temperature variations generate dilations and therefore mechanical strains, which are limited by the mechanical connections between the assembly's parts, inducing mechanical stresses. Cycle by cycle, these conditions can lead to degradation of wire-bond feet.

The samples are aged on a test bench operating under switching conditions. A general diagram of this bench is shown in Fig. 8. The test bench uses two modules to constitute a PWM Bridge loaded by an inductor (for loss minimization) that operates like a real drive inverter with respect to the electrical stress applied to IGBT dies. Closed-loop Pulse Width Modulation is applied to generate a controlled current in the IGBTs. More detailed descriptions of this test bench can be found in [2][9][10][11].

The dies are thus placed under conditions very similar to those found in industrial applications. Switching frequency can vary between 10 kHz and 40 kHz and can be used as a power cycling adjustment parameter (switching losses).

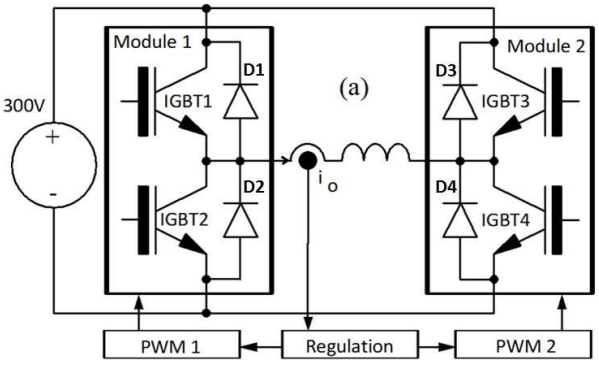

Fig. 8 : Diagram of a test bench power section

Due to the die's thermal inertia, temperature variations created by switching are negligible. The loss estimation can therefore be determined by calculating average power on each switching period over a total duration equal to the cycling period.

For one switching period, with D being the duty cycle, diode losses P_{diode} are:

$$P_{diode}(t) = (1 - D)V_d(t)i_d(t) + E_R F_{dec} \quad (1)$$

with V_d, i_d, E_R and F_{dec} are respectively the diode voltage the direct diode current, the recovery reverse energy and switching frequency.

IGBT losses P_{IGBT} are:

$$P_{IGBT}(t) = DV_{CE}(t)i_c(t) + (E_{on} + E_{off})F_{dec} \quad (2)$$

V_{CE}, i_c, E_{on} and E_{off} are the IGBT collector emitter voltage, the IGBT current, turn on and turn off energy (function of gate resistor, voltage operating, collector current). Fig. 9 shows an example of results for a rectangular current shape.

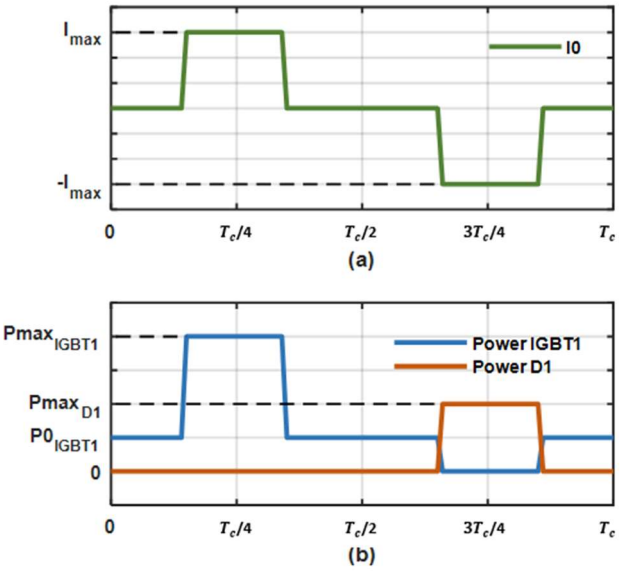

Fig. 9 : (a) Inductor current; (b) IGBT and diode losses over a period cycling

Several parameters are available for adjusting the shape and amplitude of temperature swings: load current shape and amplitude, cycling period T_c, switching period and temperature of the module base plate imposed by the cooling system.

Losses are controlled by current regulation. This action leads indirectly to the control of ΔT at the chip level. However, for a given ΔT, it is also necessary to control the minimum temperature of the cycles. This is managed via the cooling system (consisting of controlled ventilation through a water-air exchanger) which makes it possible to impose a reference temperature T_{ref} on the module base plates. Considering the test frequencies (from a few tenths of Hz to a few Hz [7]), the thermal inertia of the assembly has a filtering effect on the temperature profile [21]. The result is an almost constant temperature at the base of the modules. Thermal modeling was based on the following heat diffusion:

$$\rho C_p \frac{\partial \theta}{\partial t} - k\Delta\theta = S, \tag{3}$$

where ρ, C_p, k, θ are respectively the mass density $[kg.m^{-3}]$, specific heat $[J.kg^{-1}.K^{-1}]$, thermal conductivity $[W.m^{-1}.K^{-1}]$ and temperature variation $\theta = T\text{-}T_0$ $[^{\circ}C]$ with respect to a reference equilibrium temperature T_0. On the right-hand side of Eq. (3), S gathers electrical heat sources per unit volume. Note that the heat sources induced by mechanical transformations (e.g. viscoplastic dissipation, thermoelastic effects) were neglected. Considering the volume of the IGBT and diode dies ($\mathcal{V}_{IGBT}$ and $\mathcal{V}_{diode}$), the electrical sources S can then be written as:

$$S = \frac{P_{IGBT1}}{\mathcal{V}_{IGBT}} + \frac{P_{IGBT2}}{\mathcal{V}_{IGBT}} + \frac{P_{diode1}}{\mathcal{V}_{diode}} + \frac{P_{diode2}}{\mathcal{V}_{diode}}, \tag{4}$$

Eq. (4) represents the sources of a single module. The volume here was defined as the active part of transistors and diodes. Indeed, the edges and gate pad areas of the transistors were not included in this computation volume.

The behavior chosen for the bonding wire material (aluminum) is that of a standard thermo-elastic model in series with a temperature dependent viscoplastic model, with isotropic hardening and a linear viscosity.

The thermoelastic part of the behavior is assumed to be isotropic and its characteristic parameters (Young's modulus E, Poisson's ratio ν, linear expansion coefficient λ_{the}) are assumed to be invariant with the temperature.

The main thermoelastic constitutive equations are:

$$\varepsilon_{e_{ij}} = \varepsilon_{ij} - \varepsilon_{vp_{ij}} = \frac{1+\nu}{E}\sigma_{ij} - \frac{\nu}{E}tr(\sigma)\delta_{ij} + \lambda_{the}\theta\delta_{ij}, \tag{5}$$

where $\varepsilon_{ij}, \varepsilon_{e_{ij}}, \varepsilon_{vp_{ij}}$ are the overall, elastic, and viscoplastic strain components respectively.

The viscoplastic part of the material behavior includes isotropic hardening with an isotropic linear viscous effect in parallel. The yield function, limiting the elastic domain, reads:

$$f(\boldsymbol{\sigma}, R(p,T)) = \sigma_{eq} - R(p,T) - \sigma_e, \tag{6}$$

where $\boldsymbol{\sigma}$ is the Cauchy stress tensor, σ_{eq} the von Mises equivalent stress, R the hardening parameter depending on the accumulated viscoplastic strain p and temperature T, and σ_e the tensile yield stress.

The von Mises equivalent stress is defined by:

$$\sigma_{eq} = \sqrt{\frac{3}{2}s_{ij}s_{ij}}, \tag{7}$$

where $s_{ij} = \sigma_{ij} - \frac{1}{3}tr(\sigma)\delta_{ij}$ are the components of the deviatoric stress tensor $\boldsymbol{s}$. The equivalent viscoplastic strain rate $\dot{p}$ reads:

$$\dot{p} = \sqrt{\frac{2}{3}\left(\dot{\varepsilon}_{vp}\right)_{ij}\left(\dot{\varepsilon}_{vp}\right)_{ij}}, \tag{8}$$

where $\left(\dot{\varepsilon}_{vp}\right)_{ij}$ are the viscoplastic strain rate components. Following the Perzyna formulation [22], the viscoplastic flow rules can finally be written as:

$$\left(\dot{\varepsilon}_{vp}\right)_{ij} = \frac{\langle f(\boldsymbol{\sigma},R(p,T))\rangle^{+}}{\eta}\frac{\partial f(\boldsymbol{\sigma},R(p,T))}{\partial \sigma_{ij}}, \tag{9}$$

the operator $\langle x\rangle^{+}$ being the positive part of the variable x and η the material viscosity. The viscosity coefficient was assumed to be independent of the temperature and the viscoplastic state.

Experimental hardening curves shown hereafter (see subsection 2.4), were obtained at different temperatures and different strain rates, and led us to identify the hardening function $R(p,T)$ and estimate the viscosity η. Identification was made using a Voce's expression for R and a least-squares fitting method [23].

The identified model was expected to reveal two heat sources induced by the deformation mechanisms: a so-called thermo-elastic source S_{elast} (Eq. (10)), linked to the thermo-dilatable nature of the material, and a dissipative source S_{vp} (Eq. (11)) linked to viscoplastic irreversibility:

$$S_{elast} \approx -\lambda_{the}\theta\frac{d\boldsymbol{\sigma_I}}{dt}, \tag{10}$$

$$S_{vp} \approx \sigma_e\dot{p} + \eta\dot{p}^2, \tag{11}$$

where $\sigma_I = \mathrm{tr}(\boldsymbol{\sigma})$ is the first invariant of the Cauchy stress tensor.

Considering the present context of strong self-heating of electro-thermal origin, it appeared that the sources of mechanical origin were negligible ($S \gg 1.5\times10^{10}W/m^3$, $S_{elast} \approx 1\times10^{4}W/m^3$, $S_{vp} \approx 1.5\times10^{4}W/m^3$)The heat equation then remained the one presented in Eq. (3) with the heat source shown in Eq. (4).

To temporarily conclude the description of the mechanical behavior, let us remind that damage mechanisms are not yet included in this first model. The magnitude of the viscoplastic effects from the very first cycles on the bonding feet led us to limit the modeling to this complexity level. The often-localized damage mechanisms will be considered in a second step. The goal will then be to estimate the influence of the heterogeneous development of damage on the electric current densities and thus on the distribution of the dissipative sources of heat. The coupling loop will then be complete (Fig. 7).

The electro-thermo-mechanical context being defined, it is now possible to establish a numerical strategy to be implemented in a finite element code to characterize the ageing of wire bonds.

3. TOWARDS DIGITAL MODELLING

The complexity of the problem of ageing bonding wires does not allow us to consider an analytical solution. The use of numerical simulations via finite elements becomes a solution.

All simulations were performed with Matlab® and Comsol Multiphysics® tools. The finite element (FE) software allows us to communicate with Matlab® via a "live link". This solution has the advantage of using the computational flexibility of Matlab® to easily manipulate the models present in the finite element code library, in both preprocessing and post-processing.

The numerous parameters entering the simulation have several origins given by the multi-physical nature of the problem. These parameters are related to:

- the geometry of the system's components,
- the electro-thermo-mechanical characteristics of the constitutive materials,
- the boundary and initial conditions,
- the electrical loading (current consumed by the system or loading frequency, number of periods, etc.),
- the integration time step,
- the fineness of the spatial mesh size.

Electrical dissipation was computed using Matlab® tools. The dissipation time course was estimated using the "manufacturer" data for the IGBT module. An interpolation of the curves enabled us to calculate the heat rate involved in each of the module's semiconductors, according to the parameters of the component. This data was then inserted into the FE code to simulate the thermal problem (Eq. (3)) of the complete system using the finite element method.

All calculations regarding thermomechanical aspects were managed by the FE code. The obtained results (kinematic, stress, and temperature fields) were then transferred to Matlab® for processing and visualization.

Before presenting the modeling results, it is important to indicate how the geometries of the components were defined, how the simulations were performed, and how the material parameters necessary for the calculations were identified.

3.1. Electro-thermal simulations

First, simulations of the thermo-electric effects were carried out taking all test bench components into account. The geometry of the bench equipped with 2 IGBT modules was digitally designed using the FE code graphical interface. A preliminary numerical analysis of the self-heating effects of the complete module allowed us to no longer consider the presence of bonding wires (of low thermal inertia) in order to drastically reduce the computation time. For reasons of visibility, Fig. 10 shows the geometry of only one module. However, in the FE code the whole test bench including both IGBT modules has been simulated. Thanks to its symmetry, only half of the system was meshed for finite element calculation to reduce computation time and minimize the memory space required to store the thermal solution.

As results showed low thermal interactions between both modules, only one module was then considered for the mechanical simulation.

The primary interest of thermal simulations was twofold. First, this made it possible to determine the parameters (current shape and amplitude, switching frequency, etc.) to be applied to obtain the desired thermal profile. Second, the use of thermal data extracted from a computation made on the complete assembly (module and cooler) in the thermomechanical simulations but focused on module connectivity.

The initial conditions were those of a system in thermal equilibrium with the room temperature. The boundary conditions were of linear Fourier type, imposed on the active areas of each semiconductor. A convection coefficient was then associated with the lower surface representing the heatsink. The value of this coefficient was set to achieve the desired temperature at the measurement area used in our experimental tests. Since the module case is filled with a passivation gel that does not promote heat exchange with the external environment, we only considered exchanges via the base plate, assuming the other boundaries of the module with the surroundings to be adiabatic.

Once these assumptions were incorporated into the FE code, thermal simulations were then performed to reproduce the operating conditions obtained on the complete test bench with the same electrical parameters as those used on the experimental tests. Fig. 10 : Thermal field of the complete moduleshows an example of a 3D module thermal field.

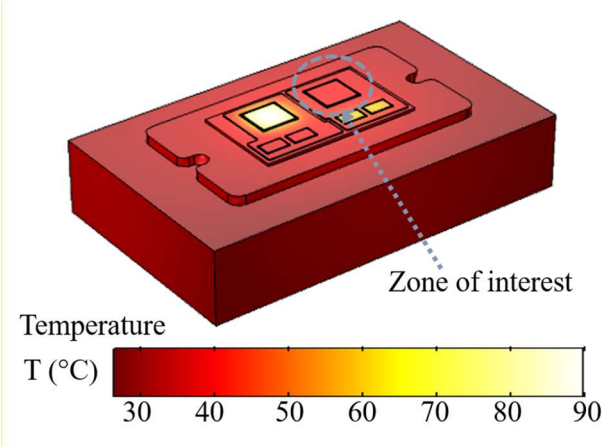

Fig. 10 : Thermal field of the complete module

Tab. 1 : Physical characteristics of module materials

	Al Bonding	*Si* Chip	*SnAg* Soldering
Heat conduction $k\ (W/m.K)$	238	130	30
Thermal expansion $\lambda_{the}(ppm/K)$	23	2.6	21

3.2. Thermo-mechanical simulations

As the objective of the numerical work is to better understand the viscoplastic transformations of the wire bonds, thermo-mechanical simulation focused on the attachment zone, thus limiting itself to soldering, chip, and bonding. This multi-material area of interest (tin/silver compound, silicon, aluminum, see Tab. 1) has very different expansion coefficients (Al/Si interface, SnAg/Si), which induces significant differential thermal expansion and therefore stress concentrations. The next section highlights that aspect. Thermal oscillations then generate a multiaxial stress state that is intense enough to induce a viscoplastic deformation of the bonding from the first quarter of cycle.

To reduce the upcoming thermomechanical calculation to a zone of interest (ZOI) surrounding the wire bond, the "coupling operators" proposed by Comsol Multiphysics® were used. In this situation, the coupling operator enabled us to recover the temperatures at the boundary of the ZOI, resulting from the

global thermal calculation of the test bench, to serve as Dirichlet thermal boundary conditions (TBCs) for the thermomechanical coupling problem focused on the wire bond region. To obtain accurate calculations when high gradients occur, the mesh size in the ZOI was refined. The coupling operator then provided the necessary interpolated data from the global mesh data. For surfaces of the ZOI in contact with the surrounding air, Fourier TBCs from the global problem were replaced by interpolated temperature (Dirichlet TBCs) derived from global computations. To reduce the computation time, a IGBT chip equipped with only one wirebond ($1.5cm$ in length and $300\mu m$ in diameter) is simulated.

The lower plane of the ZOI was considered as the reference plane regarding mechanical boundary conditions (MBCs). The center of this plane was fixed to avoid any rigid body translation, and the rotation of rigid body of this plane was prevented by blocking a movement component on one of the border points. A zero-stress normal vector was considered (Neuman MBC) for all other points of the ZOI's external surfaces in contact with the surrounding air (see Fig. 11).

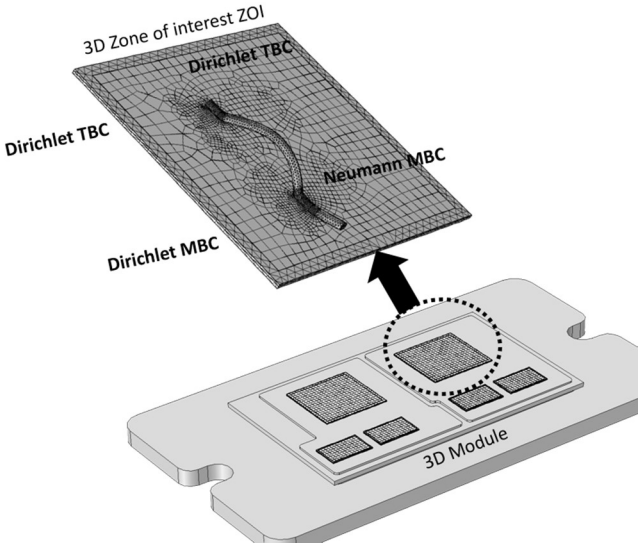

Fig. 11 : Illustration showing the role of the coupling operators; recovering the thermal boundary conditions at the ZOI boundary; and presenting the mechanical boundary conditions

To check the relevance of the Voce and Perzyna models mentioned above, six different experimental tensile tests were performed to identify the thermomechanical parameters of behavior using a TA Electroforce® 3230 mechanical testing instrument equipped with a hot-cold chamber, a 20N load cell, controlled by dedicated WinTest® 7 software.

Three temperature values (25°C, 80°C, 150°C) and two displacement speed values (25 µm/s and 250 µm/s) were combined. The temperature and cycling speed variables were selected based on the measurements taken on the test bench and the load speed resulting from the thermal cycling. At least three samples were tested in each case.

Fig. 12 shows the sample structure based on the use of an FR4 U-shaped supporting frame to (i) prevent damage or plastic deformation when handling the sample and mounting it in the testing device, (ii) achieve proper alignment of the sample, and (iii) prevent slippage in the grips during the test. The bridge between the two heads of the support frame is cut gently using a miniaturized circular saw after the sample has been mounted in the tensile device, before the test. The aluminum wire is glued to the support frame using an epoxy adhesive with high thermal performance.

Fig. 12 : Tensile test samples

The stress-strain curves obtained in the six cases are shown in Fig. 13. The first point to observe is an initial apparent stiffening of the sample that is only due to final sample realignment and straightening in the machine. This prevents measuring Young's modulus reliably. That is why samples are unloaded/reloaded after plasticity occurs. Two subsequent unloading/reloading operations were done later in the plastic zone to check the possible damage occurrence (i.e., decrease of Young's modulus). Lastly, all the samples of a given testing parameter combination provide the same stress-strain response, confirming the repeatability of the tensile test. The data obtained in the six cases can thus be compared.

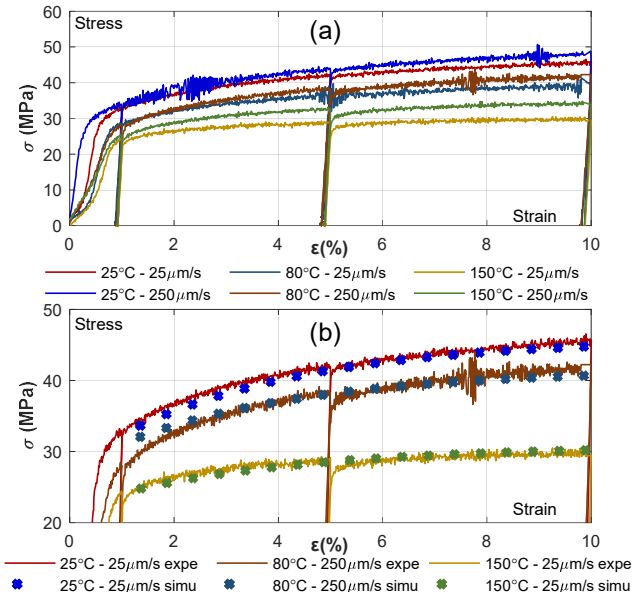

Fig. 13 : (a) Uniaxial stress-strain curves - (b) Verification of the correct implementation of hardening curves

Analysis of the six cases shows an expected result: the stress for a given strain decreases when the temperature increases. On the other hand, speed has a relatively weak influence, but a viscous effect is nonetheless observed on the plastic behavior (but not on the elastic behavior) and has been considered in the behavior models for this work. For this reasons, we chose a Perzyna-type visco-thermo-elasto-plastic model, with plastic hardening supposed to be isotropic [22]. Electro-thermo-mechanical results are described in the following sections. Finally, we note that even up to (viscoplastic) strain of about ten percent, the elastic modulus remains approximately constant, which legitimizes the fact that up to such a strain level, we neglect the effects of damage.

4. ELECTROTHERMAL RESULTS

In this section dedicated to thermal modelling, simulation results are shown. The input parameters are the heat sources of electrical dissipation (Joule effect). The heat diffusion equation then allows one to compute the temperature fields within the

module once thermal boundary conditions are defined. The first step is therefore to define the heat sources distribution.

Three different cycling frequencies, often encountered in accelerated tests, were applied: 0.1 Hz, 1 Hz, and 5 Hz [7]. The amplitude of temperature oscillations on junctions was set to ΔT_j = 50°C for all tests with a base plate module temperature of T_{ref} = 80°C (Fig. 4). To obtain the expected power cycling conditions, the electrical parameters, shown on the Tab. 2, have been adjusted for each test protocol by using quantitative thermal imaging [24] of specific modules modified for this purpose (silicone gel removed, application of black paint). These modifications allow one to improve the module emissivity and thus the measurement quality.

Tab. 2 : Power cycling parameters

Power cycling Frequency	0.1Hz	1Hz	5Hz
Mode	Sinus current	Sinus current	Trapezoidal current*
Amplitude	110A	80A	170A
Switching frequency	15.26kHz	37.23kHz	24.41kHz
Duty cycle	0.5		
Temperature base plate	71°C	65°C	52°C

* The trapezoidal current mode is a current variation form that allows to maximize the temperature cycle amplitude while respecting the maximal current in every IGBT [25]. An example of this current variation is given on Fig. 9.

These electrical parameters are used in the electro-thermal simulation. To be able to compare the temperatures measured experimentally and those obtained in simulation, a measurement zone (Fig. 14) is determined in simulation corresponding to the measurement area of the thermal camera on the test bench. The final temperature is the average of the temperatures of each element in the defined area.

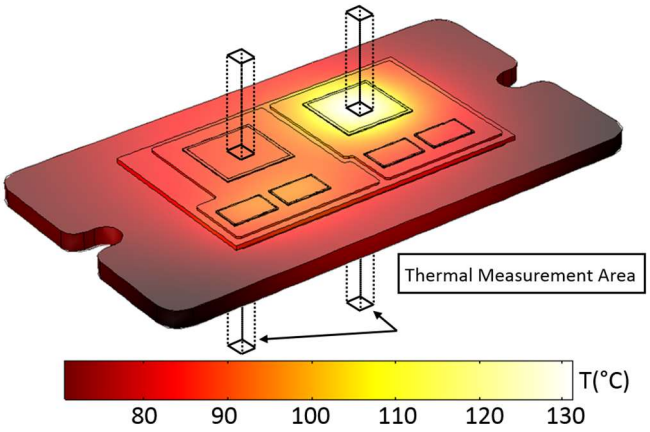

Fig. 14 : Thermal Measurement Area.

To check the relevance of the thermal computation, a comparison between FE temperature and thermal infrared measurement has been performed. Infrared thermal images were extracted from a previous study aiming at interpreting the influence of the rate of thermal loading on the ageing of connections. Experimental thermal data were then compared with the ones obtained via FE simulation in the same loading conditions.

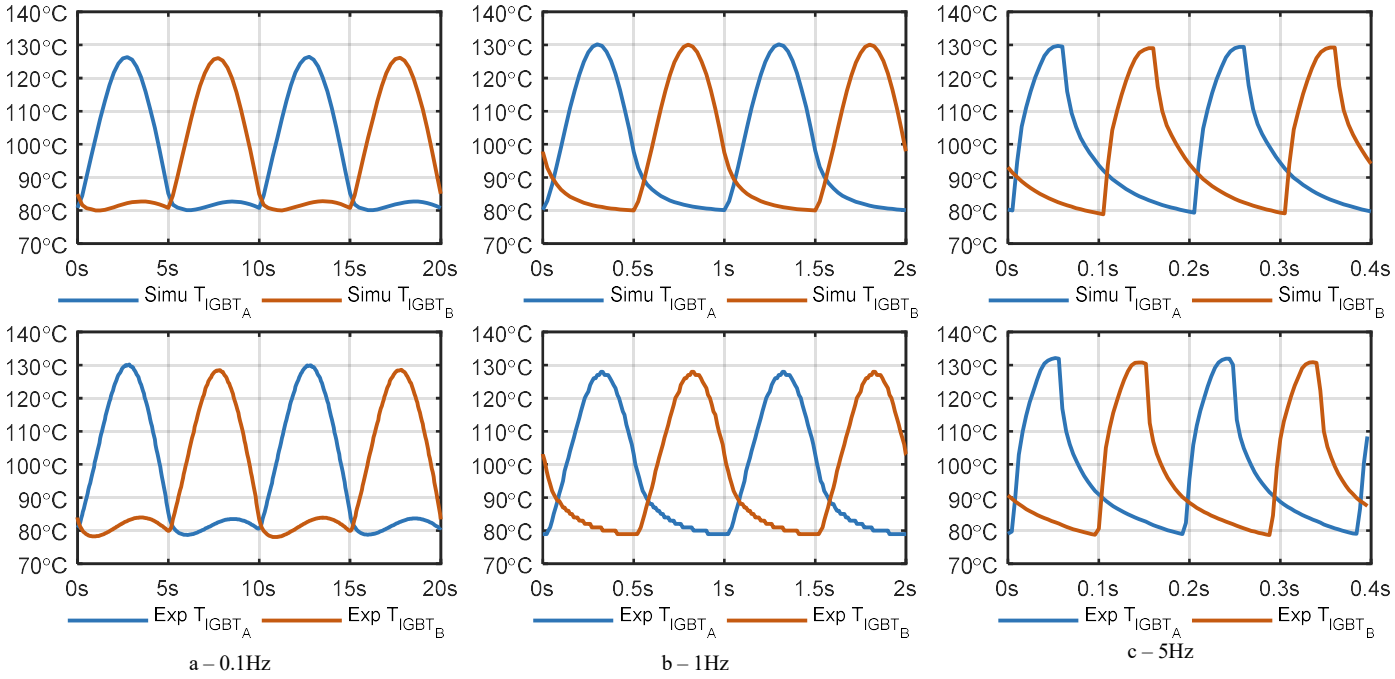

Fig. 15 : Junction temperature waveforms during Power Cycling for 0.1 Hz, 1 Hz and 5

Fig. 15 shows the shapes of the temperature oscillations, first calculated by finite element (FE) simulation applied to a complete module, then measured by infrared camera (FLIR SC6) on the specific modules. The FE computations are also required for the thermo-mechanical part and will be resumed and completed in section 5. For 0.1 Hz and 1 Hz, the load-current is sinusoidal. For 5 Hz, the current is trapezoidal, this shape being the only one able to induce a temperature variation of 50°C in accordance with the allowed current of the present test bench. In each case, the minimal temperature is close to 80°C.

Small differences between experimental and simulated data can be observed. They deal exclusively with the temperature amplitudes and do not exceed a few percent (5-10%). Several hypotheses can be put forward to explain these differences. First, the infrared thermography measurement accuracy can be evoked. The module may be poorly prepared (silicone gel removed, application of black paint, parasitic radiations, etc,..). Second, small heterogeneities of thermal characteristics in the constitutive materials may exist and are not considered in the computation.

This confrontation allows one to verify the correct integration of the heat equation, defined in Eqs (3, 4) and of the analytical model of electric losses, defined in Eqs (1, 2). These first checks are necessary before considering the analysis of mechanical stresses induced by thermal loading and responsible for the degradation of connections in power modules.

5. THERMOMECHANICAL RESULTS

The heat diffusion having a regularizing effect, one can often be satisfied in thermal FE calculation with meshes much less fine than for a mechanical or thermomechanical calculation where strong coupling mechanisms may be present. Consequently, the mesh size has been refined in the thermomechanical simulations. Indeed, we must deal with thin layers and multi-material interfaces where stress concentrations are likely to develop. From a practical standpoint, it is worth noting that the surface-to-thickness ratio is very high (e.g., chip: 10 mm × 10 mm × 70 µm). A standard mesh size allowing us to correctly characterize the thickness of the component would produce too many meshes on the surface, considerably increasing both the number of values to store and the CPU time. The method used here consists of defining a suitable mesh on the surface and then extruding this mesh through the thickness of the thin layer using a reasonable number of elements (5 for example). Fig. 16 illustrates the mesh thus created on the chip.

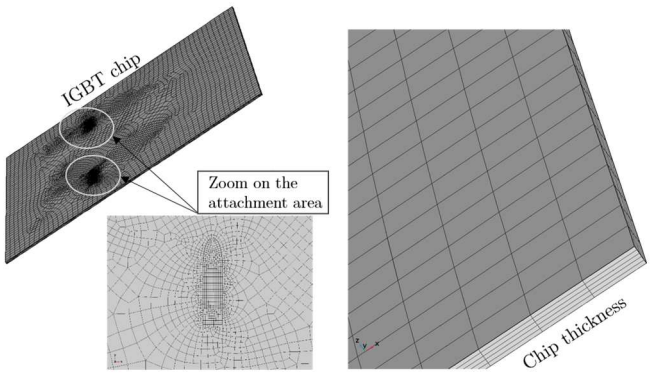

Fig. 16 : Meshing of a thin layer.

Fig. 16 shows two areas where the mesh size was refined. These are the contact surfaces of the wire-bond, areas where high stress gradients can develop.

Once the computations are made for a given cyclic thermal loading, the 3D temperature, strain, and stress fields are exported from Comsol® to Matlab® to use the data processing and graphic visualization tools of that software.

A first way to check the computation relevance is to extract the pure elastic response from the overall thermo-elasto-viscoplastic response (Eqs. (5,6,9)). To do this, it is sufficient to plot the evolution of each component over time for the stress tensor **σ** according to each elastic strain component.

For example, from Eq. (5), the component ε_{11} is derived:

$$\varepsilon_{11} = \varepsilon_{vp_{11}} + \frac{1+\nu}{E}\sigma_{11} - \frac{\nu}{E}(\sigma_{11}+\sigma_{22}+\sigma_{33}) + \lambda_{the}\theta \qquad (12)$$

where $\theta = T - T_0$, or conversely:

$$\sigma_{11} = E\left(\varepsilon_{11} - \epsilon_{vp_{11}} + \frac{\nu}{E}(\sigma_{22}+\sigma_{33}) - \lambda_{the}\theta\right) \qquad (13)$$

The correspondence, throughout the simulation duration and at any point of the structure, between σ_{11} and the quantity $(\varepsilon_{11} - \varepsilon_{vp_{11}} + \frac{\nu}{E}(\sigma_{22}+\sigma_{33}) - \lambda_{the}\theta)$ computed using the FE data, must theoretically represent a line whose slope is equal to the elastic modulus E.

In Fig. 17, the points obtained were superimposed on the theoretical response curve.

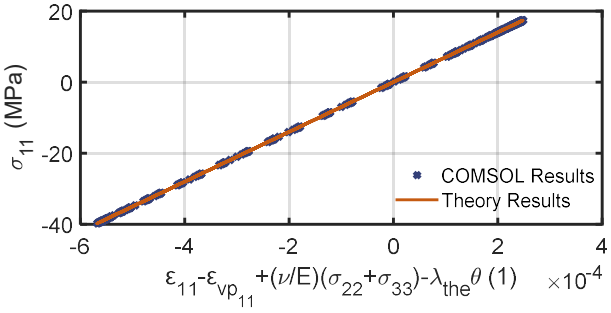

Fig. 17 : Checking thermomechanical computations: this example shows the σ_{11} component of the stress tensor.

A second way to verify the relevance of the thermomechanical results is to consider the trace of the viscoplastic strain tensor. In the model, the viscoplastic transformation is supposed to be isovolumic. Throughout thermal loading, we verified that the maximal value over the ZOI of $\mathrm{tr}(\varepsilon_{vp})$ was less than 10^{-1} . These different findings allowed one to check the correct resolution of the thermomechanical equations, defined in Eqs (5,6,9), by the FE software.

Given the complexity of the thermal loading and the composite nature of the module, a heterogeneous thermomechanical response is expected. An illustration of this heterogeneity is proposed in Fig. 18 where the distribution of the von Mises equivalent stress around the bonding feet has been plotted. The calculation shows that the stress level has reached the viscoplastic flow limit in several places.

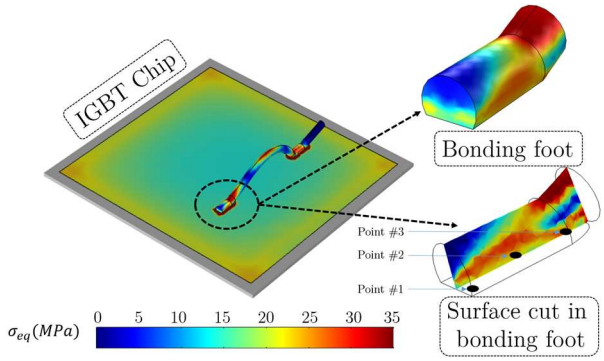

Fig. 18 : Von Mises' equivalent stress distribution in wire bond.

Another advantage given by the numerical simulation is the possibility of following the evolution of the thermal and

viscoplastic state cycle by cycle. From this perspective, three small material zones (named "points" in Fig. 19) were chosen at the interface between the bonding wire and the chip (Fig. 19). Each "point" has been indeed associated with 4 meshes. The thermomechanical data displayed in Fig. 20 are the average temperature, equivalent stress and viscoplastic strain associated with each zone. These points were chosen to better visualize the heterogeneity of the mechanical loading at the connection and to highlight the rapid increase of the equivalent viscoplastic strain (Eq. 8) since the very beginning of the cyclic loading. In Fig. 20 the evolution during the first one hundred cycles is plotted. For visibility reasons, the first 5 cycles (0-5s) and the last 5 cycles (95s-100s) are shown.

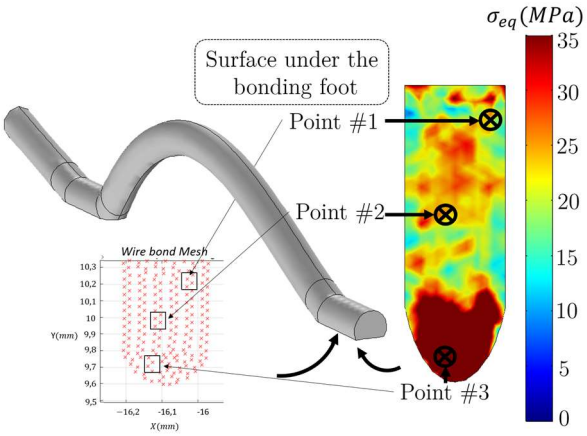

Fig. 19 : Selection of three points at the wire bond interface.

The thermal loading frequency was 1 Hz (maximum frequency of accelerated testing representative of wirebonds ageing [8]). The electrical parameters used for this simulation were identical to those indicated in Tab. 2. Fig. 20.a shows the temperature of the three points at the interface. The good diffusivity of the constituent materials leads to three temperatures that are almost identical. A gradual increase of the mean temperature per cycle can be observed. However, this warming is limited by heat losses with the surroundings by the lower elements of the module assembly (high heat capacity), themselves increasing with the temperature (Fourier TBC). Quantitatively, in this example, the mean temperature over a thermal cycle rose from about 50°C for the first simulation cycles to 80°C for the last cycles. This transient step was shortcut and symbolized by an oriented dashed line on Fig. 20. After 100 loading cycles, the thermal cycle cannot yet be considered as stabilized, (stabilization around 500 cycles to have the 80-130°C cycling). However, this number of cycles allows one to understand the fatigue mechanisms of wire bonds and justify the necessity to create a damage model while having a correct time computation (2 weeks).

In Fig. 20.b, the evolution of the von Mises stress during a cycle was plotted for the three points. Some slight differences in the stress level can be observed from one point to another. Furthermore, note that the von Mises equivalent stress by construction is a norm of the deviatoric stress tensor and must therefore always be positive. During the warming and cooling stages of the thermal cycle, tension and/or compression stresses can be observed periodically, which explains the presence of two different oscillations per cycle. Lastly, because of the gradual saturation of stresses during viscoplastic hardening (cf. Fig. 13), the von Mises equivalent stress becomes periodic rapidly. The stress-strain response stabilizes, inducing a hysteresis loop, and a viscoplastic shakedown occurs progressively.

Fig. 20.c shows the evolution of the equivalent viscoplastic strain p. Its rate must be, by construction, positive (Eq. (9)), and therefore p only increases cycle by cycle. Saturation of this variable is not possible unless the viscoplastic effects disappear (elastic shakedown). To take the large variations of p during the 100 cycles into account, two y-scales were introduced on each side of the graph. This is why the stabilization of p seems to occur, but it is only a scale effect. The monotonous growth of p depicts the irreversibility of the viscoplastic mechanisms.

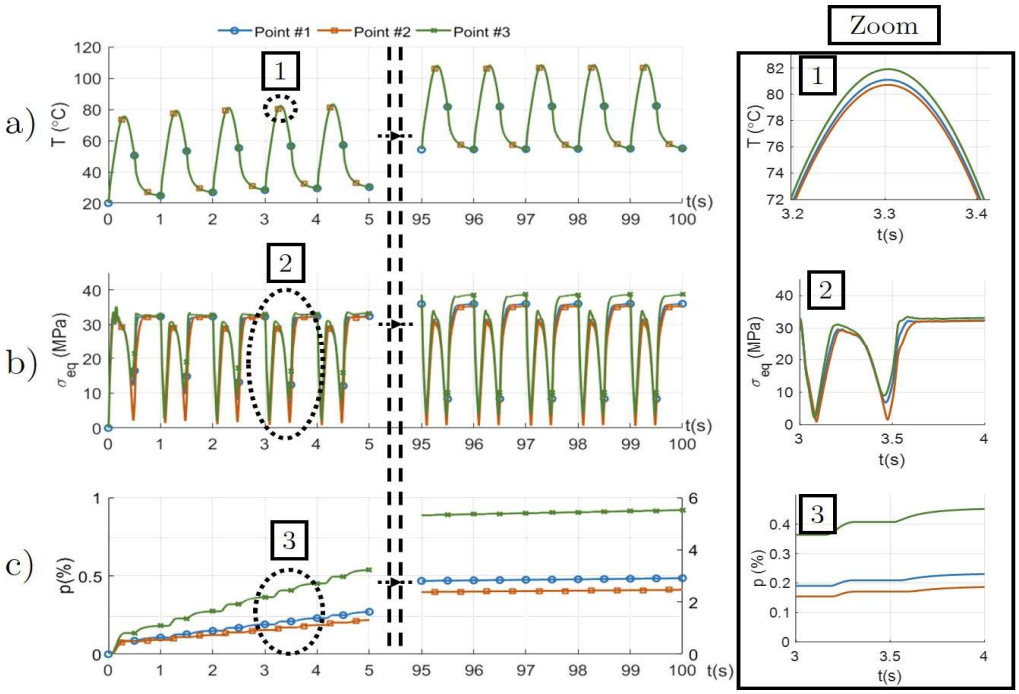

Fig. 20 : Time courses of (a) temperature, (b) von Mises equivalent stress, and (c) accumulated viscoplastic strain of the three selected points (Fig. 19) of the wire bond junctions.

The numerical calculation still allows access to each component of the stress and strain tensors. To further illustrate the complexity of thermomechanical loading for the three selected points, we plotted in Fig. 21, the paths of principal strain in the 3D space.

To make visible the strong evolution of these deformations, as before, the first and last 5 loading cycles have been plotted. We find the heterogeneous and sometimes multiaxial character of the strain. Between the two blocks of cycles, we find a strong increase of deformation whatever the point considered. During the last 5 cycles, a progressive stabilization of the strain path can be observed. As already mentioned, the presence of a hysteresis loop is associated with the growth of p. These three trajectories show significantly different evolutions in terms of both the level of strains and the shape of the loops.

Lastly, the corresponding 3 stabilized stress loops are plotted in Fig. 22. This figure confirms once again the multiaxial, heterogeneous, and irreversible character of the mechanical response of the wire bond junctions.

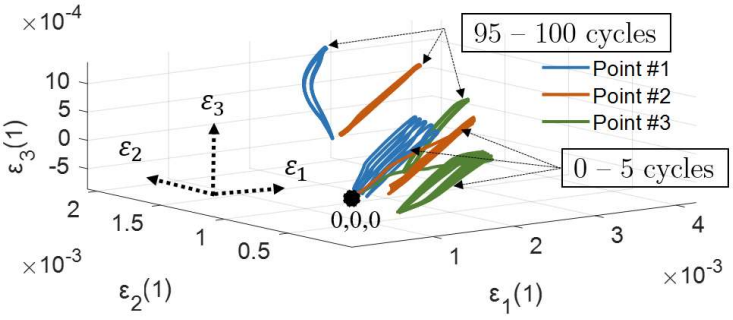

Fig. 21 : Complete strain paths of the 3 selected points in the principal strain space.

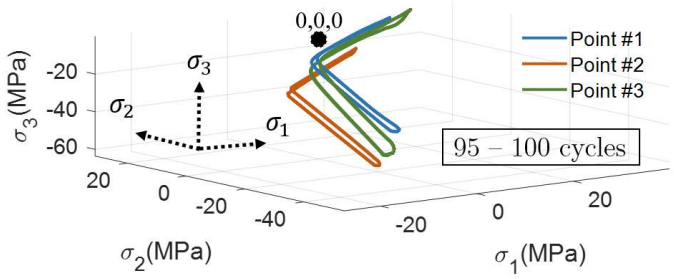

Fig. 22 : Stabilized stress loops of the three selected points in the principal stress space.

Once the cyclic stabilization is reached, if the thermal loading is not changed, the cyclic creep-fatigue mechanisms will gradually set in. The thermomechanical model, as proposed in Section 2, does not, in its current state, predict this progressive damage. The consideration of fatigue effects will be presented in a future work. The objective will be to describe the influence of the progressive damage of the component on the electric flows and thus on the distribution of the dissipative sources. In what follows, the outline of what prospective tools will be used to account for damage is briefly evoked.

6. SOME WORDS ABOUT COHESIVE ZONE MODEL

For the last thirty years, the consideration of damage in the structure design has been increasingly important. There are currently two paths to take charge of this progressive degradation of materials and structures, either in a volumetric way (continuum damage mechanics [26], or in a surface way [27]. In the future works, cohesive zone models will be associated to the volumetric finite element model already used. Indeed, cohesive-zone models (CZM), which were first introduced through the pioneering work of Barenblatt [28], are suitable for simulating fractures in a wide range of materials and to account for heterogeneities at various scales from the grain to the structure [29]. In the so-called 'cohesive-volumetric finite element' framework, CZMs are introduced at interfaces between adjacent elements of a finite element discretization (see Fig. 23 : Basic sketch of a specimen broken in uniaxial tension test by using the cohesive/volumetric finite element approach.). They have been successfully used to simulate and predict the entire fracture process from crack onset to rupture, including crack growth, propagation, potential bifurcation, multiple fracturing, etc. [30].

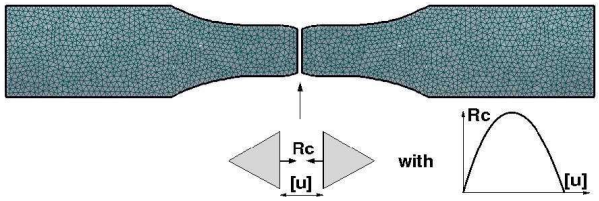

Fig. 23 : Basic sketch of a specimen broken in uniaxial tension test by using the cohesive/volumetric finite element approach.

Cohesive zone models are embedded along connected meshes and describe the traction-separation relationship as a softening curve. When the traction vanishes, the cohesive bond is broken, and the crack occurs (the resulting crack path can be complex; this figure exhibits a straight crack for sake of simplicity). The diagram Rc-$[u]$ represents the so-called

traction separation law where $[u]$ is the displacement jump and R_c the cohesive force.

7. CONCLUDING COMMENTS

This paper presents the development of a numerical modeling approach focused on bonding ageing of power modules. It seeks to systematically consider the various dissipative and multiphysical coupling mechanisms involved in ageing. The paper focuses on the modeling of electrothermal and thermomechanical effects. The main result is the identification of significant viscoplastic strains of the bonding wires from the very beginning of the loading. Locally, the loads appear to be very heterogeneous and multiaxial. The cyclic viscoplastic shakedown is reached only after several hundreds of cycles, after which the damage mechanisms become preponderant. The strategy to integrate these damage effects in the model, and their consequences on the distribution of current densities within the component, will be based in a future work on the use of cohesive zone models (CZM) [31].

8. REFERENCES

[1] K. B. Pedersen et K. Pedersen, « Dynamic Modeling Method of Electro-Thermo-Mechanical Degradation in IGBT Modules », *IEEE Trans. Power Electron.*, vol. 31, nº 2, p. 975-986, 2016, doi: 10.1109/TPEL.2015.2426013.

[2] F. Forest, A. Rashed, J.-J. Huselstein, T. Martiré, et P. Enrici, « Fast power cycling protocols implemented in an automated test bench dedicated to IGBT module ageing », *Microelectron. Reliab.*, vol. 55, nº 1, p. 81-92, 2015, doi: https://doi.org/10.1016/j.microrel.2014.09.008.

[3] O. Schilling, M. Schäfer, K. Mainka, M. Thoben, et F. Sauerland, « Power cycling testing and FE modelling focussed on Al wire bond fatigue in high power IGBT modules », *Microelectron. Reliab.*, vol. 52, nº 9, p. 2347-2352, 2012, doi: https://doi.org/10.1016/j.microrel.2012.06.095.

[4] G. Majumdar, « Power module technology for home power electronics », in *The 2010 International Power Electronics Conference - ECCE ASIA -*, 2010, p. 773-777. doi: 10.1109/IPEC.2010.5543291.

[5] Y. Yang, L. Dorn-Gomba, R. Rodriguez, C. Mak, et A. Emadi, « Automotive Power Module Packaging: Current Status and Future Trends », *IEEE Access*, vol. 8, p. 160126-160144, 2020, doi: 10.1109/ACCESS.2020.3019775.

[6] C. van der Broeck, H. Zeng, R. D. Lorenz, et R. W. de Doncker, « A Test Bench for Thermal Characterization of IGBT Power Modules Over Mission Profiles », in *PCIM Europe 2018; International Exhibition and Conference for Power Electronics, Intelligent Motion, Renewable Energy and Energy Management*, 2018, p. 1-8.

[7] U.-M. Choi, S. Joergensen, et F. Blaabjerg, « Advanced Accelerated Power Cycling Test for Reliability Investigation of Power Device Modules », *IEEE Trans. Power Electron.*, vol. 31, p. 8371-8386, déc. 2016, doi: 10.1109/TPEL.2016.2521899.

[8] B. Czerny, M. Lederer, B. Nagl, A. Trnka, G. Khatibi, et M. Thoben, « Thermo-mechanical analysis of bonding wires in IGBT modules under operating conditions », *Microelectron. Reliab.*, vol. 52, nº 9, p. 2353-2357, 2012, doi: https://doi.org/10.1016/j.microrel.2012.06.081.

[9] F. Forest *et al.*, « Use of opposition method in the test of high-power electronic converters », *IEEE Trans. Ind. Electron.*, vol. 53, nº 2, p. 530-541, 2006, doi: 10.1109/TIE.2006.870711.

[10] V. Smet, « Aging and failure modes of IGBT power modules undergoing power cycling in high temperature environments », PhD Thesis, 2010 - Université de Montpellier.

[11] V. Smet, F. Forest, J.-J. Huselstein, A. Rashed, et F. Richardeau, « Evaluation of Vce Monitoring as a Real-Time Method to Estimate Aging of Bond Wire-IGBT Modules Stressed by Power Cycling », *IEEE Trans. Ind. Electron.*, vol. 60, nº 7, p. 2760-2770, 2013, doi: 10.1109/TIE.2012.2196894.

[12] G. Coquery et R. Lallemand, « Failure criteria for long term Accelerated Power Cycling Test linked to electrical turn off SOA on IGBT module. A 4000 hours test on 1200A–3300V module with AlSiC base plate », *Microelectron. Reliab.*, vol. 40, nº 8, p. 1665-1670, 2000, doi: https://doi.org/10.1016/S0026-2714(00)00191-8.

[13] M. Held, P. Jacob, G. Nicoletti, P. Scacco, et M.-H. Poech, « Fast power cycling test of IGBT modules in traction application », in *Proceedings of Second International Conference on Power Electronics and Drive Systems*, 1997, vol. 1, p. 425-430 vol.1. doi: 10.1109/PEDS.1997.618742.

[14] T. Schutze, H. Berg, et M. Hierholzer, « Further improvements in the reliability of IGBT modules », in *Conference Record of 1998 IEEE Industry Applications Conference. Thirty-Third IAS Annual Meeting (Cat. No.98CH36242)*, 1998, vol. 2, p. 1022-1025 doi: 10.1109/IAS.1998.730271.

[15] L. Merkle, M. Sonner, et M. Petzold, « Lifetime prediction of thick aluminium wire bonds for mechanical cyclic loads », *Microelectron. Reliab.*, vol. 54, nº 2, p. 417-424, 2014, doi: https://doi.org/10.1016/j.microrel.2013.10.009.

[16] U. Scheuermann et R. Schmidt, « A New Lifetime Model for Advanced Power Modules with Sintered Chips and Optimized Al Wire Bonds » in PCIM Europe 2013, Power electronics, intelligent motion, renewable energy and energy management, 2013, p. 810-817.

[17] R. Bayerer, T. Herrmann, T. Licht, J. Lutz, et M. Feller, « Model for Power Cycling lifetime of IGBT Modules - various factors influencing lifetime », in *5th International Conference on Integrated Power Electronics Systems*, 2008, p. 1-6.

[18] L. Yang, P. Agyakwa, et M. Johnson, « A time-domain physics-of-failure model for the lifetime prediction of wire bond interconnects », *Microelectron. Reliab.*, vol. 51, p. 1882-1886, sept. 2011, doi: 10.1016/j.microrel.2011.07.052.

[19] B. Czerny et G. Khatibi, « Interface reliability and lifetime prediction of heavy aluminum wire bonds », *Microelectron. Reliab.*, vol. 58, p. 65-72, 2016, doi: https://doi.org/10.1016/j.microrel.2015.11.028.

[20] V. N. Popok, K. B. Pedersen, P. K. Kristensen, et K. Pedersen, « Comprehensive physical analysis of bond wire interfaces in power modules », *Microelectron. Reliab.*, vol. 58, p. 58-64, 2016, doi: https://doi.org/10.1016/j.microrel.2015.11.025.

[21] V. Smet *et al.*, « Ageing and Failure Modes of IGBT Modules in High-Temperature Power Cycling », *IEEE Trans. Ind. Electron. - IEEE TRANS IND ELECTRON*, vol. 58, p. 4931-4941, oct. 2011, doi: 10.1109/TIE.2011.2114313.

[22] P. Perzyna, « Fundamental Problems in Viscoplasticity », *Adv. Appl. Mech.*, vol. 9, p. 243-377, 1966.

[23] E. Voce, « A practical strain–hardening function », *Metallurgia*, vol. 51, p. 219-226, 1955.

[24] A. Chrysochoos, « Infrared thermography applied to the analysis of material behavior: a brief overview », *Quant. InfraRed Thermogr. J.*, vol. 9, nº 2, p. 193-208, 2012, doi: 10.1080/17686733.2012.746069.

[25] F. Forest, J.-J. Huselstein, G. Pellecuer, et S. Bontemps, « A Power Cycling Test Bench Dedicated to the Test of Power Modules in a Large Range of Cycling Frequency », in *PCIM Europe 2017; International Exhibition and Conference for Power Electronics, Intelligent Motion, Renewable Energy and Energy Management*, 2017, p. 1-7.

[26] J.-L. Chaboche, « Continuous damage mechanics — A tool to describe phenomena before crack initiation », *Nucl. Eng. Des.*, vol. 64, nº 2, p. 233-247, 1981, doi: https://doi.org/10.1016/0029-5493(81)90007-8.

[27] D. S. Dugdale, « Yielding of steel sheets containing slits », *J. Mech. Phys. Solids*, vol. 8, nº 2, p. 100-104, 1960, doi: https://doi.org/10.1016/0022-5096(60)90013-2.

[28] G. I. Barenblatt, « The Mathematical Theory of Equilibrium Cracks in Brittle Fracture », vol. 7, H. L. Dryden, T. von Kármán, G. Kuerti, F. H. van den Dungen, et L. Howarth, Éd. Elsevier, 1962, p. 55-129. doi: https://doi.org/10.1016/S0065-2156(08)70121-2.

[29] R. de Borst, J. J. C. Remmers, et A. Needleman, « Mesh-independent discrete numerical representations of cohesive-zone models », *Eng. Fract. Mech.*, vol. 73, nº 2, p. 160-177, 2006, doi: https://doi.org/10.1016/j.engfracmech.2005.05.007.

[30] F. Perales, F. Dubois, Y. Monerie, B. Piar, et L. Stainier, « A NonSmooth Contact Dynamics-based multi-domain solver », *Eur. J. Control - EUR J CONTROL*, vol. 19, p. 389-417, juill. 2010, doi: 10.3166/ejcm.19.389-417.

[31] V. Richefeu, A. Chrysochoos, V. Huon, Y. Monerie, R. Peyroux, et B. Wattrisse, « Toward local identification of cohesive zone models using digital image correlation », *Eur. J. Mech. - ASolids*, vol. 34, p. 38-51, juill. 2012, doi: 10.1016/j.euromechsol.2011.12.001.